Journal of Biomechanics 49 (2016) 2229–2240

Contents lists available at ScienceDirect

Journal of Biomechanics

journal homepage: www.elsevier.com/locate/jbiomech
www.JBiomech.com

Flow structures and red blood cell dynamics in arteriole of dilated or constricted cross section

Alberto M. Gambaruto [a,b,*]

[a] M. Smoluchowski Institute of Physics and M. Kac Complex Systems Research Center, Jagiellonian University, Ul. Łojasiewicza 11, 30-348, Kraków, Poland
[b] Department of Mechanical Engineering, Bristol University, Queen's Building, University Walk, Bristol BS8 1TR, UK

ARTICLE INFO

Article history:
Accepted 13 November 2015

Keywords:
Computational haemodynamics
Microcirculation
Red blood cells
Cell migration
Wall shear stress
Secondary flow structures
Dilated vessels
Constricted vessels

ABSTRACT

Vessel with 'circular' or 'star-shaped' cross sections are studied, representing respectively dilated or constricted cases where endothelial cells smoothly line or bulge into the lumen. Computational haemodynamics simulations are carried out on idealised periodic arteriole-sized vessels, with red blood cell 'tube' hematocrit value=24%. A further simulation of a single red blood cell serves for comparison purposes.

The bulk motion of the red blood cells reproduces well-known effects, including the presence of a cell-free layer and the apparent shear-thinning non-Newtonian rheology. The velocity flow field is analysed in a Lagrangian reference frame, relative to any given red blood cell, hence removing the bulk coaxial motion and highlighting instead the complex secondary flow patterns. An aggregate formation becomes apparent, continuously rearranging and dynamic, brought about by the inter-cellular fluid mechanics interactions and the deformability properties of the cells. The secondary flow field induces a vacillating radial migration of the red blood cells. At different radial locations, the red blood cells express different residence times, orientation and shape.

The shear stresses exerted by the flow on the vessel wall are influenced by the motion of red blood cells, despite the presence of the cell-free layer. Spatial (and temporal) variations of wall shear stress patters are observed, especially for the 'circular' vessel. The 'star-shaped' vessel bears considerable stress at the protruding endothelial cell crests, where the stress vectors are coaxially aligned. The bulging endothelial cells hence regularise the transmission of stresses on the vessel wall.

1. Introduction

Whole blood is composed of plasma (~55% by volume) that is mostly water, and holds in suspension several types of cells that include red blood cells (RBCs, erythrocytes), white blood cells (WBCs, leukocytes) and platelets (PLTs, thrombocytes), as well as smaller particles such as microvesicles, amongst others. The proportion of blood occupied by RBCs is referred to as the hematocrit (HCT), and is normally ~40–45% by volume, while WBCs occupy ~1/600 and PLTs occupy ~1/800 of total cell volume (Popel and Johnson, 2005). The RBCs tend to form aggregates at low shear rates while disaggregation is determined mainly by mechanical shear forces, giving rise to the observed non-Newtonian shear-thinning rheology of blood. RBCs are also deformable and their change in shape, alignment and distribution at different shear rates and vessel calibre, all contribute to the non-Newtonian rheology (Popel and Johnson, 2005; Lipowsky, 2005).

Individual particles suspended in a medium will preferentially migrate towards the centre of the vessel due principally to velocity gradients that generate a lift force (Saffman, 1965). Deformability of particles has also been studied in relation to the migration behaviour (Nix et al., 2014). In whole blood, the radial migration of RBCs towards the centre of the vessel results in a cell-free layer close to the vessel wall, the effect of which is more pronounced in small vessels. This phenomenon leads to the well-known Fåhræus and Fåhræus–Lindqvist effects, which describe respectively the decrease in hematocrit in small vessels and the dependence of apparent viscosity of blood on vessel size (Lipowsky, 2005; Pries et al., 1992; Popel and Johnson, 2005). As a consequence of the RBCs migration, WBCs and PLTs are effectively cast towards the vessel walls.

At different vessel diameters and shear rates, the RBCs will form stable aggregates or rearrange in a regulated manner due to the inter-cellular fluid mechanics interactions (Freund and

* Correspondence address:Department of Mechanical Engineering, Bristol University, Queen's Building, University Walk, Bristol BS8 1TR, UK.
E-mail address: alberto.gambaruto@bristol.ac.uk

http://dx.doi.org/10.1016/j.jbiomech.2015.11.023
0021-9290/

Orescanin, 2011; Pries et al., 1992). These configurations result in a complex interplay between local viscosity, dissipation through secondary flows and RBC deformability, influencing the cell-free layer height and the apparent viscosity of blood. It has been suggested in Omori et al. (2015) that the apparent viscosity and the cell-free layer thickness may be primarily determined by macroscopic parameter, such as vessel diameter, flow rate, and hematocrit, rather than by precise microscopic cellular mechanics, such as the membrane mechanics and fluid motion around the cell. Despite this, it is observed that high RBC concentration and intercellular fluid mechanics interactions are responsible for the outward radial migration of white blood cells (Takeishi et al., 2014) and platelets, with evident physiological relevance. Experimental studies have also outlined blood mass transport mechanisms under both physiological and pathological conditions (Lima et al., 2008). The detailed flow motion and cell mechanics therefore play an important role in the physiological functions, and is studied in the current work. Inter-cellular interactions other than those due to the fluid mechanics may include electric potentials, biological and biochemical processes, such as ligand–receptor bonds, however these will not be considered in the present study.

While most studies of computational haemodynamic microcirculation employ circular pipes as idealised models of the vessel geometry, it is the aim of the present study to consider the effects of more complex geometrical definitions. To this end, an endothelial cell layer is explicitly modelled. Some works of 2-dimensional flow of a single RBC over an idealised endothelial surface layer in narrow vessels have reported interesting differences in the transmission of stresses with respect to flow in circular pipes (Secomb et al., 2001, 2002), with evident implications on mechanotransduction signalling. In the present work, 3-dimensional simulations in larger vessels and with a physiological hematocrit level are carried out.

The paper is organised as follows. The case studies simulated are detailed in Section 2, together with a brief outline of the numerical method employed. Results and discussion of simulations of red blood cell microcirculation are presented in Section 3, while conclusions are given in Section 4. For completeness, an Appendix is also provided with details of the numerical method.

2. Methods

Haemodynamic microcirculation is investigated by means of numerical simulations, providing data at high spatial and temporal resolution. Three case studies are chosen to investigate the flow field that arises due to the presence and interaction of RBCs, the resulting radial migration of the RBCs and the stresses that are exerted on the vessel wall. These case studies are effected on geometric idealisations of the micro-vasculature, with increasing level of detail:

- Case 1: 'dilated' geometry (circular cross section)
  diameter $=22.2$ μm, length $=49.6$ μm, number of RBCs $=1$, hematocrit $=0.7\%$, total simulation time $=1.1$ s
- Case 2: 'dilated' geometry (circular cross section)
  diameter $=22.2$ μm, length $=49.6$ μm, number of RBCs $=36$, hematocrit $=24\%$, total simulation time $=1.1$ s
- Case 3: 'constricted' geometry (star-shaped cross section)
  diameter $=17$–25 μm, length $=49.6$ μm, number of RBCs $=36$, hematocrit $=24\%$, total simulation time $=1.1$ s

The vessels are periodic and the initial setup for Cases 2 and 3 are shown in Fig. 1. All Cases have the same fluid volume content, however Case 3 has an increased wall surface area due to the configuration of the bulging endothelial cells, resulting in a smaller hydraulic diameter.

As noted by Popel and Johnson (2005), as an arteriole is dilated its lumen is approximately circular (Cases 1 and 2), while during arteriolar constriction the lumen will be more irregular due to the bulging of endothelial cells and may result in a 'star-shaped' cross section (Case 3). It is important to note that the 'constricted' and 'dilated' configurations do not correspond to the same vessel in the present work. These two configurations are instead chosen for comparison purposes to have the same fluid volume content.

The geometry of Case 3 includes the presence of endothelial cells which are modelled as rigid and static, represented by an undulating vessel wall. The endothelial cells are arranged in a structured manner and are described by trigonometric functions resulting in: cell length (coaxial direction) $=24.8$ μm, cell width (azimuthal direction) $=11.2$ μm, cell height (radial direction) $=4$ μm. While endothelial cell dimensions and shape are presented quite disparately in the literature, the results reported in Fukushima et al. (2003), Garipcan et al. (2011), Ohashi and Sato (2005), and Yamaguchi et al. (2000) were used as inspiration to define the geometry of Case 3.

The flow is driven by imposing a constant pressure drop $\Delta p = 10$ Pa, driving the flow in the negative z-axis direction. An approximately constant flow rate is attained, which is representative of the physiological state of microvascular flow due to low Womersley number (Popel and Johnson, 2005). Due to the RBCs motion, interaction and aggregation behaviour, the flow resistance at any instant will fluctuate, resulting in small oscillations in flow rate (or pressure, Freund and Orescanin, 2011).

2.1. Mathematical models and numerical method

The Navier–Stokes equations, which describe the motion of fluids, represent the mathematical model used to simulate haemodynamics microcirculation. Individual red blood cells are simulated by coupling a structural model for the cell membranes to the Navier–Stokes equations, through the addition of body force terms. A mesh-free particle method is used to solve the equations in Lagrangian reference frame, well suited to the complex motion and interaction of the suspended cells in plasma. In this method, the domain is discretised by particles, each representing a volume of fluid h_0^3, where h_0 is the particle spacing (in a Cartesian layout). The mesh-free particle method employed is based on the Moving Particle Semi-implicit (MPS) method (Koshizuka et al., 1998; Tsubota and Wada, 2010; Imai et al., 2010; Alizadehrad et al., 2012; Gambaruto, 2015). Further details about the numerical method are outlined in the Appendix and in Gambaruto (2015).

The final form of the incompressible Navier–Stokes equations to be solved is:

$$\frac{1}{\rho}\frac{D\rho}{Dt}+\nabla\cdot\mathbf{u}=0$$
$$\frac{D\mathbf{u}}{Dt}=-\frac{\nabla p}{\rho}+\nu\nabla^2\mathbf{u}+\mathbf{g} \quad (1)$$

where $\frac{D}{Dt}$ denotes the material derivative with respect to time, $\mathbf{u}$ is the velocity, p is the pressure, $\mathbf{g}$ is the external body force per unit mass, and ρ and ν are respectively the fluid density and the kinematic viscosity. The body force term $\mathbf{g}$ accounts for the structural model for the cell membranes, in specific a spring network model is adopted. The RBC membranes are described by a mesh of triangle elements, which connectivity defines the spring network elements. The discretisation of the domain into particles and the cell membrane by a spring network are shown in Fig. 2.

The body force term $\mathbf{g}$ consists in three force terms:

$$\mathbf{g}=\mathbf{f}^t+\mathbf{f}^b+\mathbf{f}^r \quad (2)$$

where $\mathbf{f}^t$ accounts for in-plane tension and compression forces of the springs, $\mathbf{f}^b$ accounts for out-of-plane bending forces, and $\mathbf{f}^r$ is a repulsive force which ensures that no particles cross the cell membranes and provides a simple lubrication force. Various constitutive laws for springs have been used to model cell membranes (Fedosov et al., 2010; Bessonov et al., 2014; Fedosov et al., 2010; Tsubota and Wada, 2010; Imai et al., 2010). The spring elements discussed in Gambaruto (2015) and Bridson et al. (2003) are adopted in the present work; shown in Fig. 2 while formulas are given in Appendix A.4.

2.2. Red blood cell shape as an ellipsoidal best-fit

In order to study the RBC deformed shapes, a least-squares best-fit approximation to an ellipsoid is used. This is computed using a proper orthogonal decomposition (POD) of points discretising the cell membrane, resulting in the gyration tensor (Alizadehrad et al., 2012; Pan et al., 2010):

$$G=\frac{1}{N_v}\sum_{i=1}^{N_v}(\mathbf{x}_i-\overline{\mathbf{x}})(\mathbf{x}_i-\overline{\mathbf{x}})^T \quad (3)$$

where N_v is the number of vertices of the spring network mesh, and $\overline{\mathbf{x}}=\frac{1}{N_v}\sum_{i=1}^{N_v}\mathbf{x}_i$ is the centre of mass of the membrane vertices. The gyration tensor G is a 3×3 symmetric positive definite matrix, with real eigenvalues $\lambda_1\geq\lambda_2\geq\lambda_3$ and corresponding orthonormal eigenvectors ξ_1,ξ_2,ξ_3, that are respectively related to the length squared (consequently 'energy') and orientation of the ellipsoidal axes. For example, RBCs at rest have $\lambda_1=\lambda_2>\lambda_3$, with ξ_1,ξ_2 defining the biconcave plane of symmetry and ξ_3 indicates the axis of rotational symmetry.

The stretch ratio as the ellipsoid major to minor axes length squared, hence (λ_1/λ_3), and the angle between the minor axis and RBC direction of motion, hence

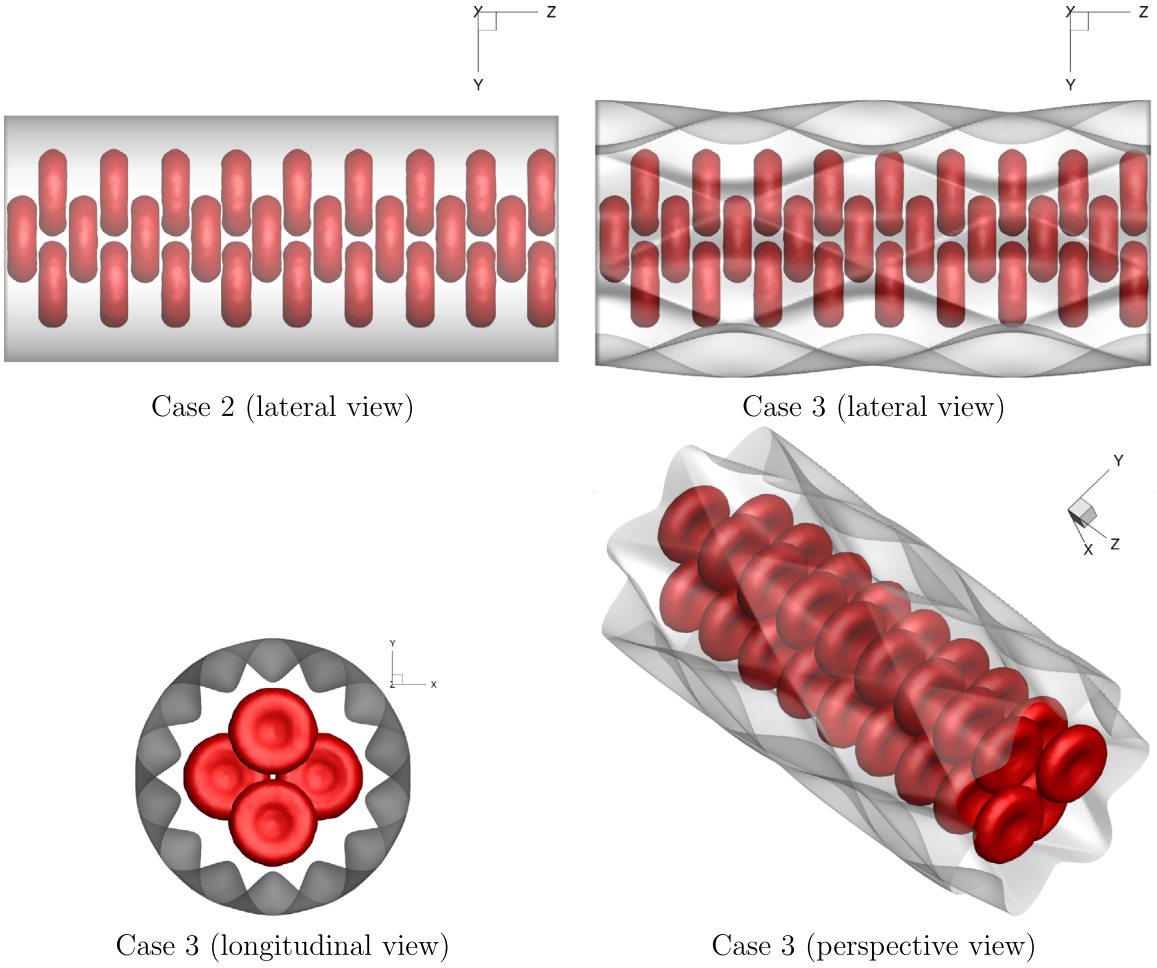

Fig. 1. Initial setup for Cases 2 and 3. The RBCs are aligned to have the minor axis of the biconcave shape aligned to the vessel coaxial direction (z-axis). The RBCs are numbered incrementally in the coaxial direction to facilitate the analysis of their relative motion. The initial setup for Case 1 is identical to Case 2, save that only the first RBC is modelled. A pressure drop $\Delta p = 10$ Pa is applied to drive the flow in the negative z-axis direction.

$\measuredangle(\langle \mathbf{u} \rangle_{RBC} \cdot \xi_3)$, will be used to analyse the shape and motion of the RBCs. Note $\langle \cdot \rangle$ indicates average value.

2.3. Simulation setup: parameters and coefficients

The material properties of the fluid (plasma and red blood cells) were set as density $\rho = 1000$ kg m^{-3}; dynamic viscosity $\mu = 0.001$ Pa s. While representative, these are simplifications since the cytoplasm viscosity is approximately five times that of plasma (Fedosov et al., 2010).

The particle discretisation was set to $h_0 = 0.4$ μm following Imai et al. (2010), while similar sizes have been used in Alizadehrad et al. (2012) ($h_0 = 0.46$ μm) and Tsubota and Wada (2010) ($h_0 = 0.26$ μm). Each cell membrane was also discretised at the same resolution by an unstructured mesh, resulting in $\sim$ 1000 vertices and $\sim$ 2000 triangle faces, considered adequate following the convergence results in Omori et al. (2011). The initial biconcave shape of RBCs was given as an analytic function proposed in Fedosov et al. (2010). The response of the RBCs to static stretch tests reported in Suresh et al. (2005) has been used as benchmarking of the spring network model employed (Gambaruto, 2015).

Typically WBCs do not adhere to healthy arteriolar endothelium, and furthermore flowing WBCs (and PLTs) are not expected to affect the flow field significantly due to their small concentration (Popel and Johnson, 2005). As such, neither WBCs nor PLTs have been modelled in the present study.

3. Results and discussion

Statistics of the RBCs motion are presented in Tables 1 and 2 and are computed for three equispaced radial partitions of the computational domains: 'core', 'middle' and 'external' regions, defined by the maximum recorded radial location of any RBC centre of mass during the simulations. The mean RBC velocity magnitude, $\langle |\mathbf{u}| \rangle_{RBC}$, is substantially less for Case 3 compared to Case 2 due to the increased wall surface area of the vessel.

The mean velocity magnitude of the RBCs and of the entire domain (both plasma and RBCs), at time T = 1.1 s, are given in Table 3, from which we note that the RBCs have a greater velocity than the bulk flow, in agreement with the Fåhræus effect. Comparing Cases 1 and 2, we note that the higher hematocrit flow gives rise to a larger apparent viscosity, and hence a reduced mean flow rate.

In the following analysis and presentation of results, an interpolation of data from the scattered particles to a Cartesian mesh was employed when necessary. This is performed when providing cross sectional plots, streamline integration and time averaged measures. In specific, a Shepard interpolation (Shepard, 1968) was used: an inverse distance weighting where the weights are given by d^{-p}, where d is the Eucledian distance and p is the 'power parameter'. A large power parameter $p = 3.5$ was used, resulting in a moderately smooth Voronoi tessellation of the field variables.

3.1. Dynamics of multiple RBCs

The profile of velocity magnitude at two cross sections at time snapshot $T = 1.1$ s, as well as the time averaged velocity profile, are shown in Fig. 3, in which the characteristic blunt profile of a non-Newtonian shear-thinning rheology emerges. We note that the two cross section profiles at the time snapshot $T = 1.1$ s differ

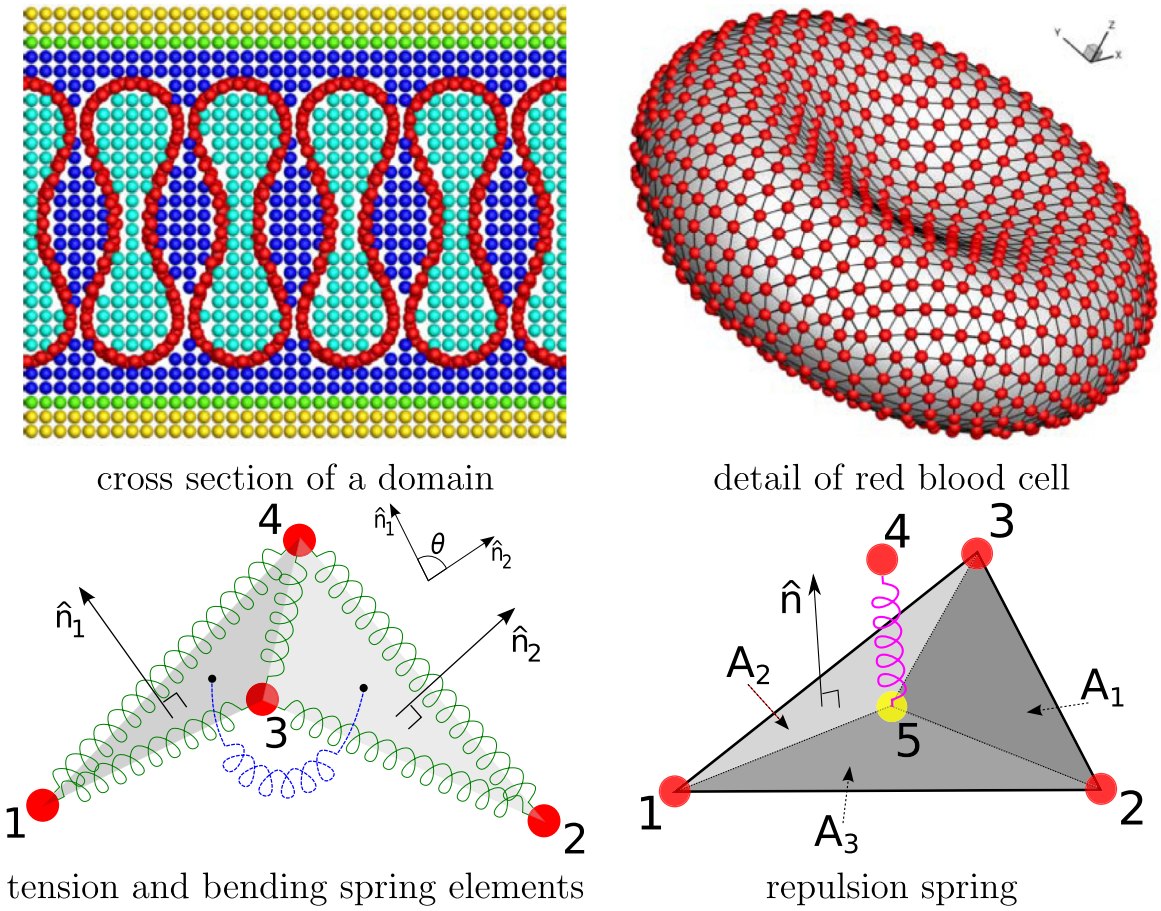

Fig. 2. *Top left*: cross section of example domain at the start of the simulation. The particles are arranged in a Cartesian fashion and the red blood cell membranes are then inserted, subsequently removing abutting particles. The different particles colouring highlights the different classifications of the particle species: yellow='ghost', green='wall', blue='plasma', azure='cytoplasm', red='membrane'. *Top right*: detail of a single red blood cell membrane, showing the particle discretisation and the spring network connectivity. *Bottom left*: pictorial representation of two triangle mesh elements of the membrane sharing a common edge, showing the spring elements resisting both tension/compression and bending. *Bottom right*: pictorial representation of a triangle element of the membrane, showing the spring that generates the repulsive forces. The red particles 1,2,3 make up the cell membrane, particle 4 is the abutting particle, while the yellow point (no. 5) defines the location of action of the repulsive force. (For interpretation of the references to colour in this figure caption, the reader is referred to the web version of this paper.)

Table 1
Statistics of red blood cell radial migration: the 'flux count' is the average number of times a RBC crosses into a different radial partition; the 'residence time' is the percentage time a RBC resides in each radial partition. The standard deviation of the 'flux count' provides information of the spread of the data. The statistics are computed for the simulation period $T=0.1$–1.1 s, excluding transients at the start of the simulation ($T \leq 0.1$ s) related to the initial setup.

Radial partition	Flux count (mean)	Flux count (standard deviation)	Residence time (%)
Case 2			
Core ($0-2.9\mu m$)	5.2	4.2	18
Middle ($2.9-5.8$ μm)	10.0	4.2	38
External ($5.8-8.7$ μm)	4.6	3.2	44
Case 3			
Core ($0-2.7\mu m$)	3.5	4.0	18
Middle ($2.7-5.4$ μm)	8.3	4.3	35
External ($5.4-8.1$ μm)	4.6	3.8	46

due to the heterogeneous distribution of the RBCs, as seen also in Figs. 7 and 8. A coaxial view along the vessels, shown in Fig. 3, highlights the presence of a cell-free layer near the vessel wall while the RBCs are located in the central region of the vessel. The apparent viscosity in the central region is greater than for the cell-free layer, and subsequently the blunt velocity profile is observed from the time averaged results. Good agreement in both height of the cell-free layer and velocity profiles for Case 2 are reported (Freund and Orescanin, 2011; Alizadehrad et al., 2012).

The time averaged statistics of RBC orientation and stretch, based on the best-fit ellipsoid shape, are presented in Table 2 for both Cases 2 and 3. The emerging trend is an increase in both stretch ratio and angle subtended, with the radial location of the RBC. These observations together with Figs. 7 and 8, indicate that RBCs will flatten and expose a greater surface area to the lumen wall with increased proximity, while in the core flow region the shape is more complex ('parachute' or 'slipper' shaped) and the orientation is more coaxial, lending a propensity for RBCs to cluster and fit in the wake of the upstream RBCs. Similar trends in orientation and deformed shapes of RBCs are reported in Alizadehrad et al. (2012).

3.2. Dynamics of single RBC

For comparison purposes to better understand the motion and interaction of multiple RBCs, the behaviour of a single RBC is studied through Case 1, and the results are presented in Fig. 4. We note that the RBC migrates from an initial displaced position to the centreline of the vessel, and along this trajectory it undergoes swinging motion (Abkarian et al., 2007; Meßlinger et al., 2009), before attaining a stable parachute shape at the centreline. Note that the radial location of the RBC after reaching the stable

Table 2
Left to right, mean values for: velocity magnitude for the RBCs; stretch ratio of ellipsoid shape; angle between red blood cell mean velocity and ellipsoid minor axis; mean resultant internal membrane force magnitude. The standard deviation of the measures is given in the square brackets, to provide information of the spread of the data. The statistics are computed for the simulation period $T=0.1$–1.1 s, excluding transients at the start of the simulation ($T \leq 0.1$ s) related to the initial setup.

Radial partition	$\langle \lvert \mathbf{u} \rvert \rangle_{RBC}$ (mm/s)	$\langle \lambda_1/\lambda_3 \rangle$	$\left\langle \angle(\langle \mathbf{u} \rangle_{RBC} \cdot \xi_3) \right\rangle$ (deg)	$\langle \lvert \mathbf{g}_m \rvert \rangle$ (pN)
Case 2				
Core ($0-2.9\mu m$)	4.3 [0.98]	2.3 [0.58]	65 [15.7]	2.6 [0.59]
Middle (2.9 – 5.8 μm)	4.2 [0.13]	2.8 [0.21]	74 [4.1]	2.6 [0.05]
External (5.8 – 8.7 μm)	2.9 [0.67]	3.2 [0.73]	75 [16.9]	2.4 [0.54]
Case 3				
Core ($0-2.7\mu m$)	3.3 [0.76]	2.2 [0.53]	62 [16.6]	2.6 [0.60]
Middle (2.7 – 5.4 μm)	3.2 [0.17]	2.7 [0.23]	75 [3.5]	2.7 [0.06]
External (5.4 – 8.1 μm)	2.2 [0.44]	3.1 [0.62]	76 [14.6]	2.5 [0.47]

Table 3
Results for time snapshot $T=1.1$ s. Left to right, mean values of velocity magnitude for both the RBCs and the entire domain, and the pseudo-shear rate $\dot{\gamma}$. The mean velocity of each RBC was found to be effectively coaxial. The analytic solution is given by Poiseuille equation, such that $u(r)=\frac{R^2\Delta p}{4\mu L}\left(1-\left(\frac{r}{R}\right)^2\right)$, where R and L are respectively the vessel radius and the length, μ is the fluid viscosity, and Δp is the applied pressure drop. It should be noted that the radius R, used in the analytic solution, has been adjusted due to the initial Cartesian discretisation of the domain (Gambaruto, 2015).

Radial partition	$\langle \lvert \mathbf{u} \rvert \rangle_{RBC}$ (mm/s)	$\langle \lvert \mathbf{u} \rvert \rangle_{entire\ domain}$ (mm/s)	$\dot{\gamma}$ (1/s)
Analytic solution	–	3.3	144
Case 1	5.9	3.3	143
Case 2	3.7	2.6	115
Case 3	2.8	1.8	79

configuration is marginally off-centre, due to limitations in the numerical spatial discretisation.

Once the RBC has attained the parachute shape, mid-plane cross sections of velocity magnitude and pressure are extracted, as well as the streamlines of the flow field relative to the RBC. The cross section of velocity magnitude shows a locally blunted profile in the vicinity of the RBC, similar but not as emphatic as when many RBCs are present, as in Case 2. The cross section of the pressure (excluding the pressure drop imposed as boundary condition) shows an increase in the flow resistance as the RBC passes, hence higher pressure on the vessel wall at its location, and a high pressure gradient across the RBC in order to drive it.

As detailed in Omori (2012, 2015), the capillary number Ca represents the ratio of the viscous force to the elastic force and can be used to classify the motion an RBC about its axes under a shear flow. The capillary number is given by

$$Ca=\frac{\mu\alpha\dot{\gamma}}{G_s} \tag{4}$$

where μ is the plasma viscosity, α is the characteristic length (radius of a sphere with the RBC volume), G_s is the membrane shear modulus (Omori et al., 2011), $\dot{\gamma}=\langle \lvert \mathbf{u} \rvert \rangle/D$ is the pseudo-shear rate, and D is the effective vessel diameter. As noted also in Freund and Orescanin (2011) and Meßlinger et al. (2009), the viscosity ratio of cell cytoplasm to plasma can also affect the RBC motion. For Case 1, $Ca \approx 0.2$ which is considered a low value, and the swinging motion due to the shear flow occurs as the RBC deforms and rotates about an oscillating axis. Snapshots of the swinging motion are shown in Fig. 4, and their occurrence can be clearly identified in the plot of stretch ratio. The time for the swinging motion increases as the RBC migrates closer to the vessel centreline, due to the smaller shear rate present. It is interesting to note that the mean resultant internal membrane force magnitude, $\langle \lvert \mathbf{g} \rvert \rangle$ (Eq. (2)), increases steadily during the swinging motion, rapidly falling once the RBC has completed a swing and recovers to a more discoid shape. In the final steady parachute configuration the RBC assumes at the centre of the vessel, the mean resultant internal membrane force is approximately of the same magnitude as the peaks during the swinging motion. The parachute configuration hence exhibits a higher mean resultant membrane force than a more discoid shape.

3.3. Radial migration of RBCs

As noted above for all Cases studied, the RBCs migrate to the central region of the vessel and form a cell-free layer at the vessel wall. While the simulation Case 1 for the single red blood cell shows that a stable configuration is attained, in Cases 2 and 3 the RBCs continuously alter in shape and relative positions. The radial location of each RBC centre of mass is tracked during the simulations, and some mean measures are reported in Table 1, specifically the 'flux count' and the 'residence time'. The 'residence time' describes the percentage of time that the RBCs spend in each of the radial partitions. The 'flux count' is the average number of times a RBC cross over into a different radial partition. It should be noted that the 'middle' region interfaces with both 'core' and 'external' regions, and we would expect a flux count approximately twice as large in comparison.

The results for Cases 2 and 3 are similar, with the flux count ~4–5 for each radial partition. For both Cases, the greatest residence time is attributed to the 'external' region and least in the 'core' region. From Table 2 we also note that in the 'external' region the mean RBC velocity is less than the 'core' and 'middle' regions, influencing the higher residence times.

The standard deviation of all measures reported in Table 2 is smallest for the 'middle' radial partition. This result indicates that the RBC characteristics tend to be more homogeneous, and consequently that this radial partition serves as a traversing region for RBCs migration, which occurs with consistent attributes and characteristics.

The measures of flux count and residence time, together with the orientation and stretch ratio of the RBCs discussed above, highlight the mechanisms that promote both mixing and exchange processes combined. In Fig. 5 the radial location of a selection of RBCs is plotted for both Cases 2 and 3 to show that various trajectories may be observed, including RBCs that reside solely in one region or alternatively traverse the vessel either partially or entirely. For both Cases 2 and 3, RBCs could be identified that had similar radial migration behaviour, though the RBC numbering itself was not the same to indicate that the dynamics was not dependent on the initial setup of the simulations. Small oscillatory motion is observed along each trajectory, highlighting the complex flow field both generated and traversed by the RBCs. From these plots the transient behaviour due to the initial simulation setup is identifiable in the time window $T=0$–0.1 s, and data during this period is discarded in all analyses.

3.4. Secondary flow field

The simulation of Case 1 resulted in the migration of the single RBC to a stable configuration at the centre of the vessel, after an initial phase of swinging motion. On the other hand, from the simulations of Cases 2 and 3 we observed that the RBCs cluster in the central region of the vessel and form an aggregate. This aggregate differs from the rouleaux structures that are obtained at lower shear rates, in that it is a continual dynamic interplay

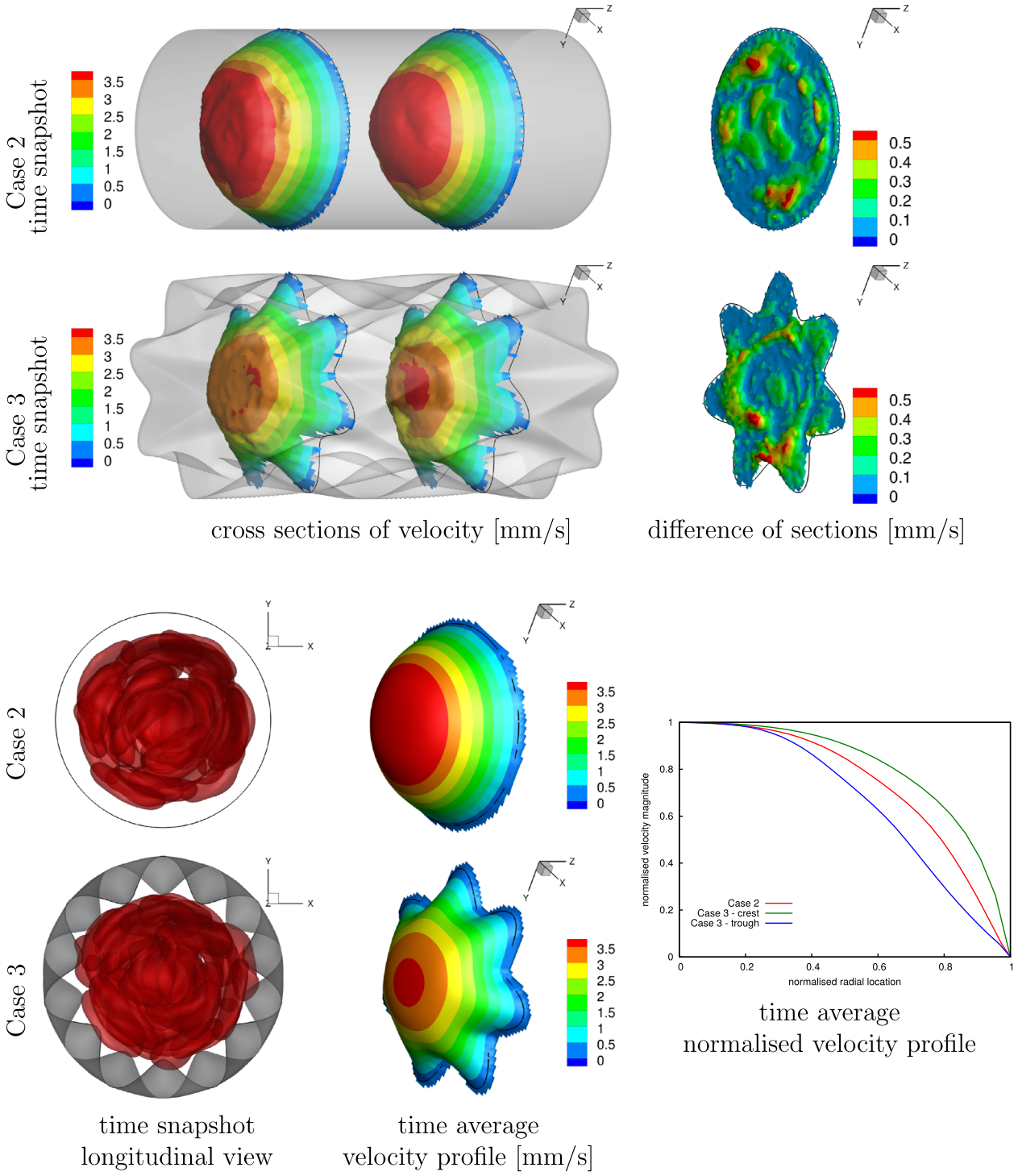

Fig. 3. Results for the time snapshot $T=1.1$ s and time averaged velocity profiles. *Top*: cross sections of velocity (mm/s), extracted at location 25% and 75% of the vessel lengths, and the differences in these sections. The flow direction is right to left. *Bottom left*: longitudinal views along the vessels, highlighting the cell-free layer formed by the RBC migration to the centre of the vessel. *Bottom centre*: time averaged velocity cross section profiles. *Bottom right*: line plot of normalised velocity as a function of radial position. Note that for Case 3, the radial position goes from vessel centre to the top of the endothelial cells (crest), and alternately from centre to the bottom of the cells (trough).

between the cells, rearranging ceaselessly due to their deformability property and the complex flow field.

The fluid velocity field can be considered as a linear superposition of a dominant (coaxial) and secondary (relative) flow field, hence:

$$\mathbf{u}_{fluid} = \mathbf{u}_{coaxial} + \mathbf{u}_{relative} \tag{5}$$

Taking a Lagrangian reference frame relative to an individual RBC, with the coaxial velocity given by its mean speed, then the secondary flows relative to it are given by $\mathbf{u}_{relative} = \mathbf{u}_{fluid} - \langle \mathbf{u}_{coaxial} \rangle_{RBC}$. Streamlines of the true and relative flow fields are shown in Fig. 6, for Case 3 at time $T=0.74$ s, for three RBCs that have distinct radial migration behaviours. While the streamlines in the true flow field will generally point to the direction of motion, in the Lagrangian frame, the streamlines may change direction depending if the RBC is moving faster or slower along the vessel than the surrounding

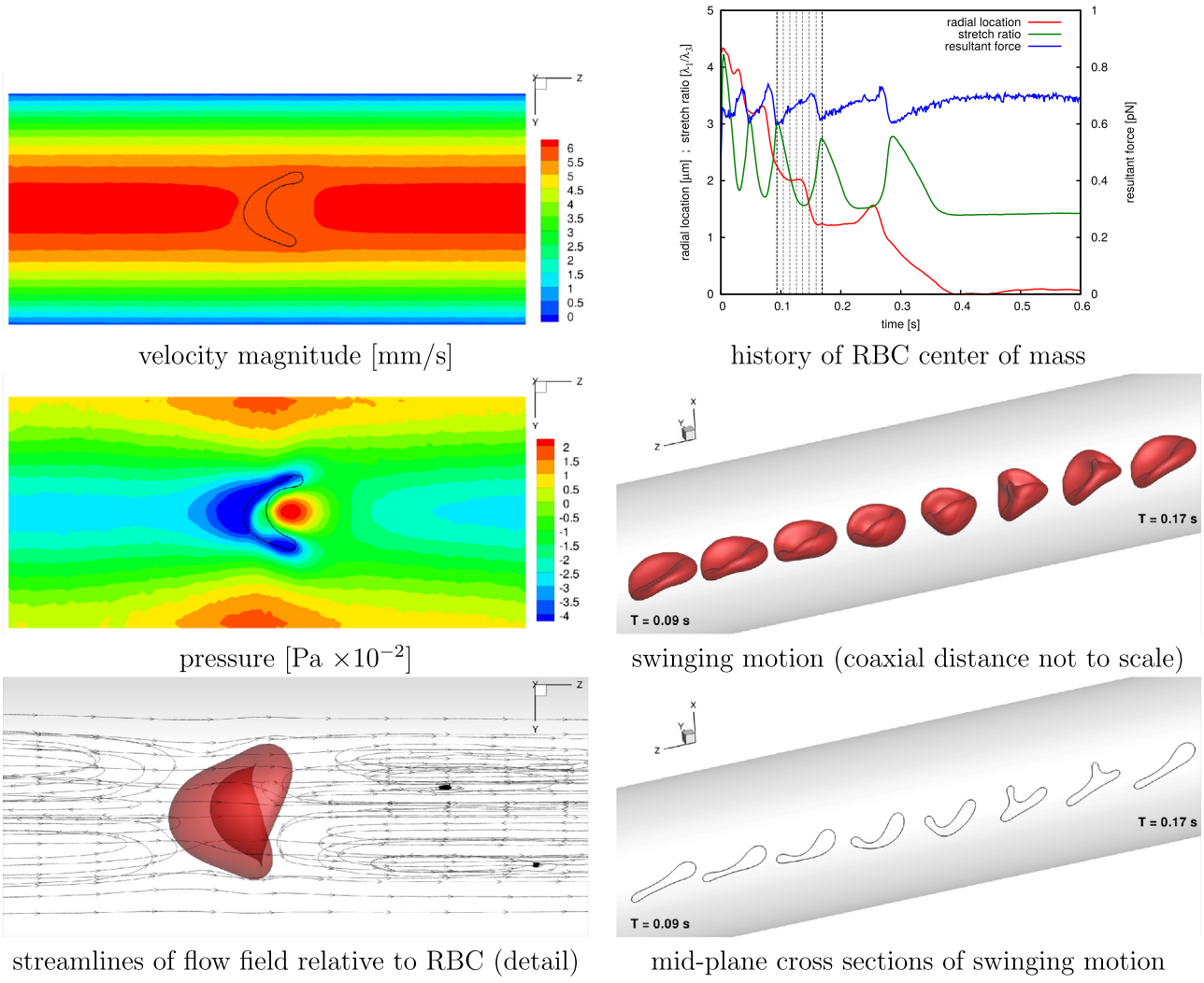

Fig. 4. Results for the simulation of Case 1. *Top left* (the flow direction is right to left): velocity magnitude and pressure are for the snapshot time $T=0.6$ s, in the mid-plane cross section. The pressure shown is computed in Step.6 of the numerical scheme (see Appendix A.2), hence does not include the pressure drop boundary condition to drive the flow ($\Delta p = 10$ Pa). *Bottom left* (the flow direction is right to left): the streamlines of the flow field relative to the RBC are for the snapshot time $T=0.6$ s, from which a vortex ring in the wake of the cell is visible. *Top right*: the RBC centre of mass history shows correspondence between the radial location, stretch ratio and mean resultant internal membrane forces. Equispaced time intervals are marked on the plot during the time window $T=0.09$–0.17 s, corresponding to the RBC swinging motion shown (at the bottom right).

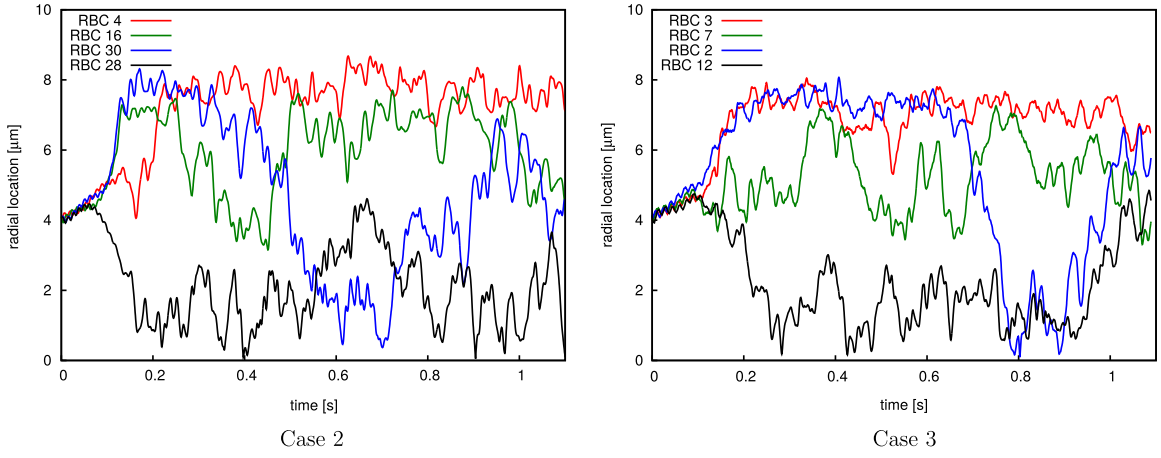

Fig. 5. History of radial location of the different RBCs during the simulation. Simulation transients related to the initial setup are visible during $T \leq 0.1$ s. RBCs with similar radial migration behaviour can be identified for both Cases 2 and 3 (see colour scheme), however the RBC identification numbering is different to indicate that the dynamics are not dependent on the simulation setup. RBCs are seen to: reside only at a large radial location (red), reside only at a small radial location (black), entirely traverse the admissible range of radial location (blue), traverse a partial distance of the admissible range (green). (For interpretation of the references to colour in this figure caption, the reader is referred to the web version of this paper.)

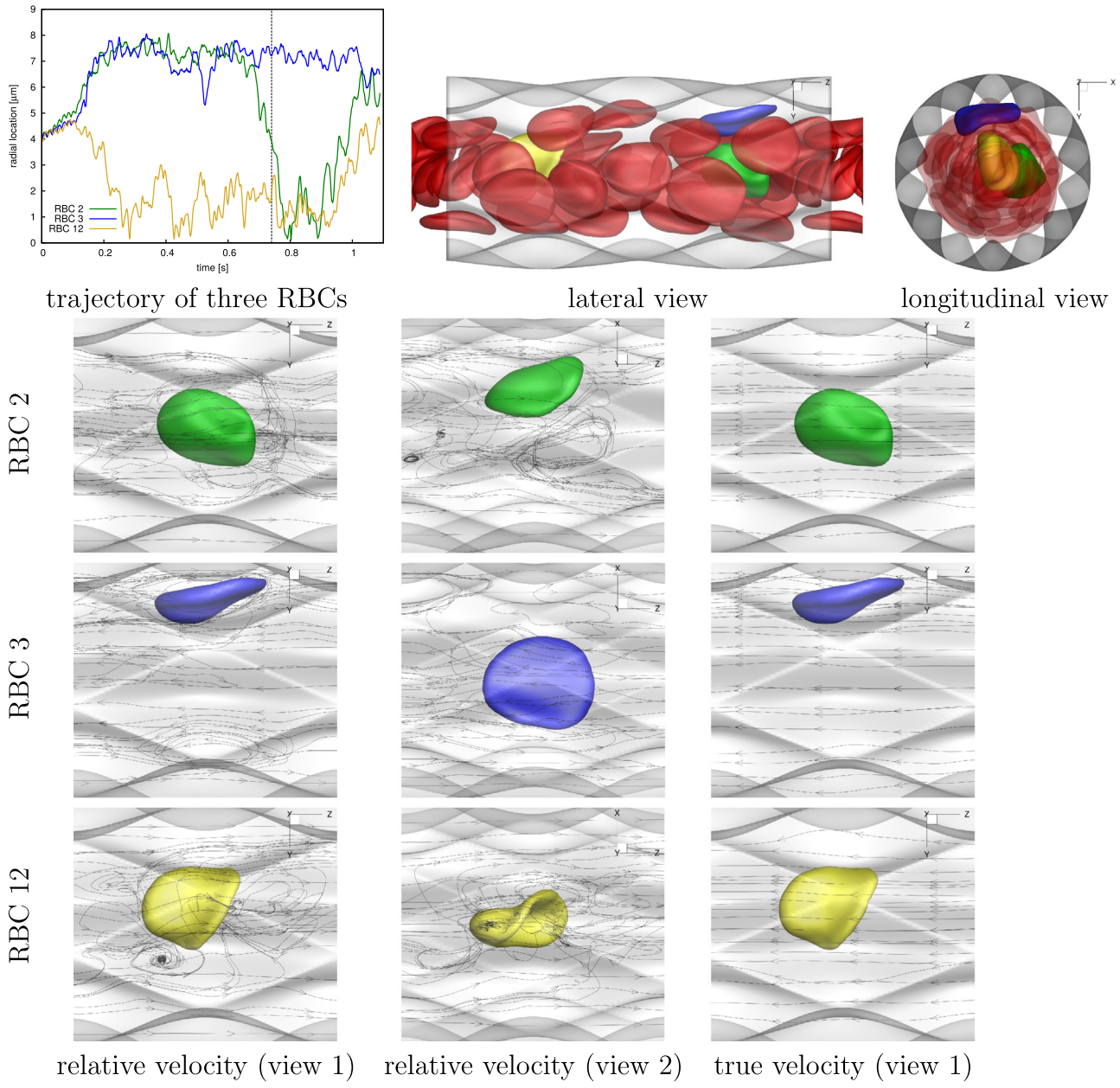

Fig. 6. Results for Case 3 at the time snapshot $T=0.74$ s. The results are colour coded to maintain correspondence of the RBCs. *Top left*: plot of radial location history for the three RBCs, showing the time instance chosen, coinciding with RBC 2 migrating radially towards the centre of the vessel. *Top right*: lateral and longitudinal views of the vessels. *Bottom*: streamlines of relative and true velocity flow field, in two perpendicular views. The RBC motion is right to left, as are the streamlines of the true velocity. The streamlines of relative velocity highlight a complex secondary flow field, due to the inter-cellular fluid mechanics interactions and cell deformability properties.

fluid. In specific if the streamlines in the relative flow field have direction upstream-to-downstream (hence left to right in Fig. 6), the RBC is moving faster coaxially than the surrounding fluid, and conversely if the streamline direction is reversed. For all the RBCs shown in Fig. 6, we note that the RBCs are in general travelling faster than their surroundings, with exception of RBC 3 which is located at a large radial location and is travelling slower than the core flow but faster than the near-wall flow.

The streamlines of the relative flow field furthermore expose vortex structures and regions of recirculating flow, which are evidence of the inter-cellular fluid mechanics interplay that result in RBC clustering and dynamic aggregate formation. For RBC 2, which is migrating towards the core region at time $T=0.74$ s, the relative flow field is generally towards the vessel centre, with a number of vortex structures manifesting in the core flow region while the external region is relatively coaxial. For RBC 3, which maintains a radial location in the external region of the vessel, the relative flow field suggests a rotational, possibly tank-treading motion of the cell. For RBC 12, which maintains a radial location in the core region of the vessel, the shape is such that a large trailing vortex is generated while the tip of the cell is subjected to the wake of a preceding RBC. The streamlines that describe these dynamics in fact traverse other RBCs not shown in Fig. 6, and the streamlines of the relative flow therefore also describe the relative motion of the suspended cells and not only the plasma.

For comparison purposes, the streamlines of the relative flow field computed for Case 1 are shown in Fig. 4. A vortex ring structure in the wake of the RBC is present, which due to the periodic boundary conditions loops and extends to the front of the RBC again. It can be foreseen that additional RBCs lying in this wake would be affected and result in inter-cellular fluid mechanics

interactions that define the individual and compound motion of the suspended cells.

3.5. Wall shear stress

The wall shear stress (WSS) is computed as:

$$\boldsymbol{\tau}_w = \left(\boldsymbol{\tau}\cdot\vec{\mathbf{n}}\right) - \left(\left(\boldsymbol{\tau}\cdot\vec{\mathbf{n}}\right)\cdot\vec{\mathbf{n}}\right)\vec{\mathbf{n}} \tag{6}$$

where $\vec{\mathbf{n}}$ is the unit outward normal to the wall surface (computed using a least-squares approximation), and $\boldsymbol{\tau} = \mu(\nabla\mathbf{u} + \nabla\mathbf{u}^T)$ is the extra stress assuming a Newtonian fluid. The velocity gradient tensor has been computed using the discrete gradient operator detailed in Appendix A.3.

The WSS acts tangential to the plane of the wall, in the opposite direction to the flow, and is the viscous traction force exerted by the flow on the wall. By integrating the WSS vector field on the vessel wall, we obtain the surface shear lines (SSL), which indicate the direction of the flow velocity vector in the limit as the wall is approached. Both WSS and SSL are shown in Fig. 7 for the time snapshot $T = 1.1$ s. For Case 3, the WSS magnitude is observed to be larger at the protruding crests of the endothelial cells, and substantially lower at the bottom of the cells, in the troughs along neighbouring cell boundaries. The crests of the cells are subjected to higher flow velocity gradients (see Fig. 3), and greater interactions with the RBCs. The SSL are seen to meander around the endothelial cells, while at the crests of the endothelial cells the SSL are aligned coaxially. For Case 2, the pattern of WSS magnitude is to a greater extent dictated by the interaction of RBCs that leave a footprint of stresses exerted on the vessel wall (Freund and Vermot, 2014; Gambaruto, 2015), and the SSL largely run coaxially. The SSL are seen to locally deviate from the coaxial direction as the flow field is disturbed by the motion of the RBCs. The WSS and SSL have a greater degree of spatial (and subsequently also temporal) variation in both magnitude and direction when no endothelial cells are modelled.

The mean WSS magnitude at the time snapshot $T = 1.1$ s and the time average results are respectively: $\langle WSS\rangle_{T=1.1\ s} = 1.22$ Pa, $\langle WSS\rangle_{\langle T\rangle} = 1.09$ Pa for Case 2 and $\langle WSS\rangle_{T=1.1\ s} = 1.86$ Pa, $\langle WSS\rangle_{\langle T\rangle} = 1.82$ Pa for Case 3. In Fig. 7, the time averaged WSS and SSL for Case 3 is also presented, and we report that for Case 2 a uniform time averaged WSS is obtained with the SSL running coaxially. On comparing the time averaged results to those of the time snapshot, it is evident that RBCs and the resulting complex flow field affect the stress distribution that the fluid exerts on the vessel wall,

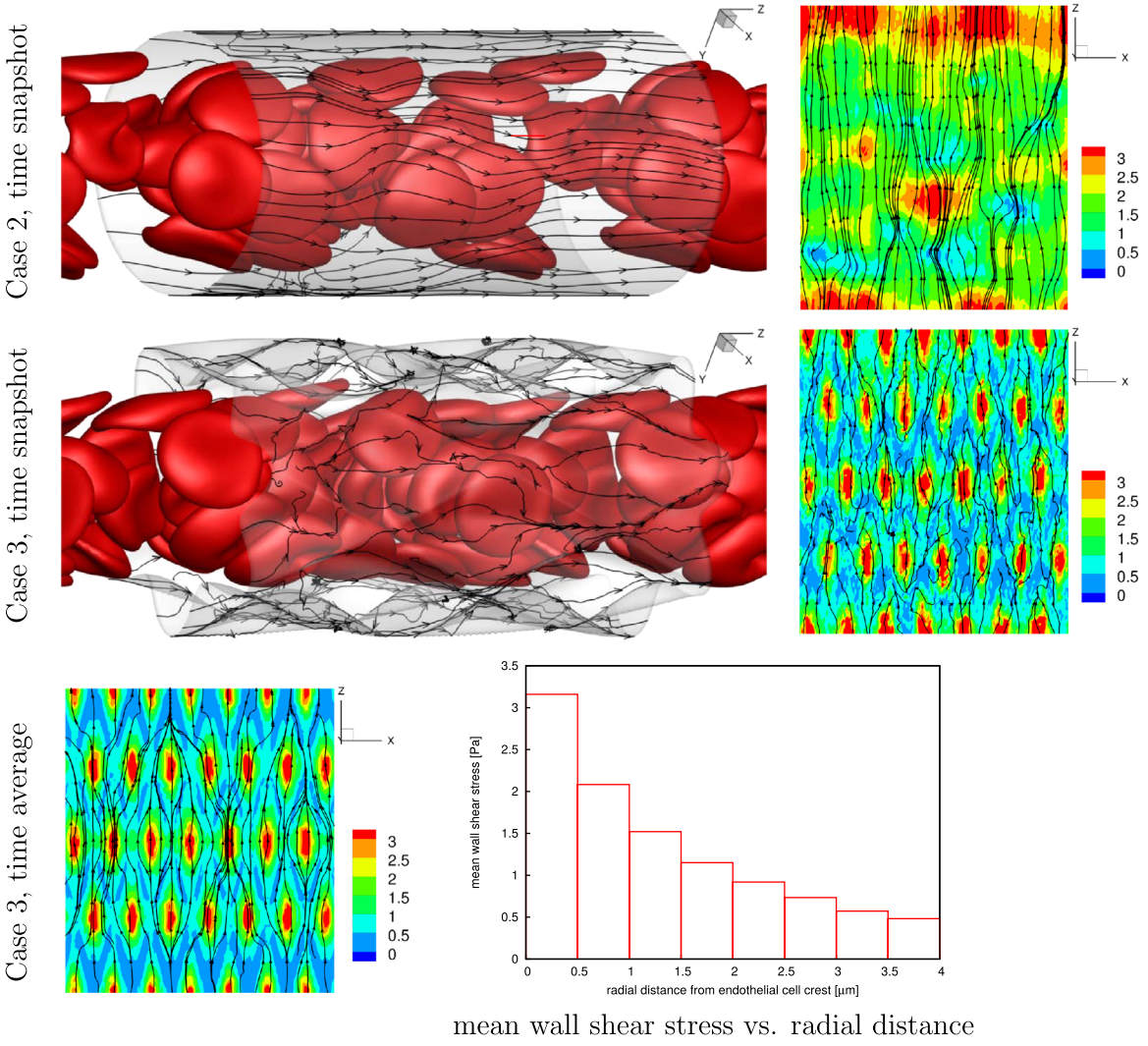

Fig. 7. Wall shear stress (WSS) at the time snapshot $T = 1.1$ s and time averaged solution. The integral of the WSS on the vessel wall defines the traction paths on the vessel surface, termed the surface shear lines (SSL). *Top left*: RBCs and SSL, where the flow direction is right to left. *Top right*: plot of WSS magnitude [Pa] and SSL, obtained by unwrapping the vessel (hence the *x*-axis here represents the azimuthal direction), where the flow direction is top to bottom. The WSS magnitude and SSL are seen to be disturbed by the RBCs and the bulging endothelial cells. *Bottom left*: time averaged solution for Case 3, showing a regular pattern of WSS and SSL. *Bottom right*: histogram of time averaged WSS distribution on the endothelial cell surfaces for Case 3 as a function of the radial distance, from cell crest to trough.

especially for Case 2. The spatial and temporal distribution of the forces that the flow exerts on the vessel wall, related to the motion of the suspended cells in plasma, may influence the mechanotransduction signalling processes. The time averaged WSS distribution on the endothelial cell surfaces for Case 3 as a function of the radial distance, from cell crests to troughs, is plotted in Fig. 7. The histogram shows an inverse relationship, indicating that the endothelial cell crests bear the brunt of the stresses, shielding the bottom of the cells.

3.6. Membrane forces

The magnitude of resultant internal membrane forces per unit mass, $|\mathbf{g}|$ (Eq. (2)), is an indicator of the extent the local fluid mechanics is affected (or perturbed) by the cell membrane. In fact $|\mathbf{g}|$ is the external body force acting on the Navier–Stokes equations (Eq. (1)), being the instrument to express and simulate the RBC membranes in the numerical method. Let us write the resultant internal membrane forces as $\mathbf{g}_m = \mathbf{g} \cdot M$, where $M = \rho \cdot h_0^3 = 10^3 \cdot (0.4 \times 10^{-6})^3 = 6.4 \times 10^{-17}$ kg is the mass of the particles that discretise the domain, considering the spatial resolution and fluid density used in the present study. The magnitude of the forces, $|\mathbf{g}_m|$, are shown in Fig. 8 for time $T = 1.1$ s, and can be seen to be greatly inferior to the static stretch used tests to characterise the RBC membrane stiffness properties in Suresh et al. (2005), Fedosov et al. (2010), Imai et al. (2010), and Gambaruto (2015).

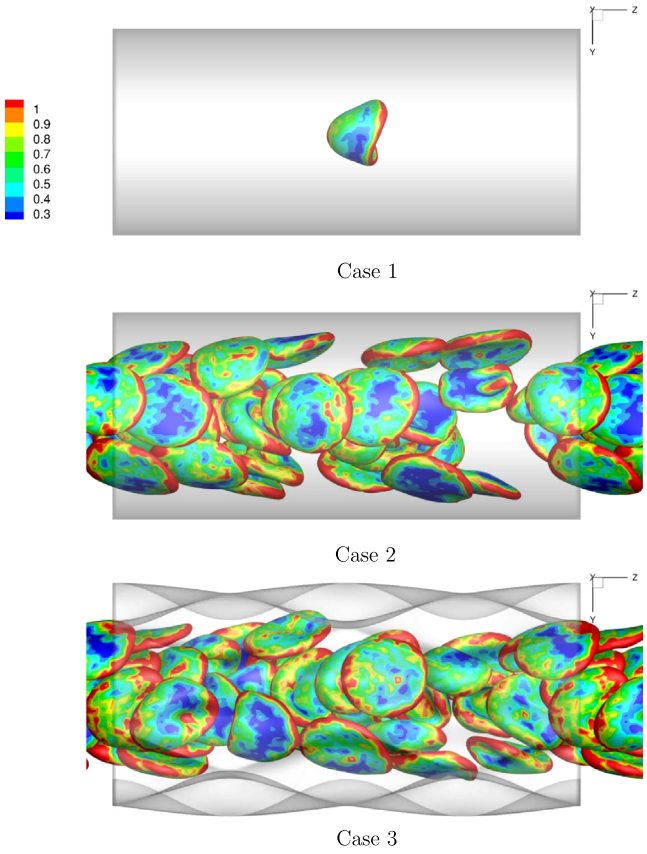

Fig. 8. Resultant internal membrane force magnitude [pN], at the time snapshot $T = 1.1$ s. The flow direction is right to left. These are the non-equilibrium forces, $\mathbf{g}_m = \mathbf{g} \cdot M$, computed in Eq. (2) that act on the fluid in Eq. (1), multiplied by the mass of the particles $M = 6.4 \times 10^{-17}$ kg. It is evident that the regions of higher curvature contribute to the largest values. The orientation of the RBCs is such as to expose a larger surface area with proximity to the vessel wall, and a more tight knit cluster in the central region of the vessel.

The greatest resultant forces arise at regions of higher curvature, and for RBCs located closer to the vessel walls these larger bending forces appear along the rim of the discoid shape that the RBCs assume, especially at the leading and trailing edges. For RBCs in the central region of the vessel, the dynamic aggregate formations consist in RBC deformed configurations such as 'parachute' or 'slipper' shapes, and the higher curvature regions again appear at the leading and trailing edges. The average forces during the simulation period are reported in Table 2, from which rather uniform values emerge, with marginally greater values for Case 3 as the vessel wall is approached. The 'middle' region reveals a markedly smaller standard deviation and hence more uniform distribution. In fact from Table 2 and Fig. 4, the 'middle' radial region consistently reports the smallest standard deviation of all the measure, suggesting that this region may serve as a transition domain in the radial migration, during which the shapes of the RBCs assume similar configurations, unlike the 'core' and 'external' regions.

4. Conclusion

The dynamics of red blood cells (RBCs) are studied for three simulation cases of idealised periodic arteriole-sized vessels of increasing modelling complexity. The cases studied may be treated as a comparison between dilated and constricted vessels, in which endothelial cells are respectively modelled as flat or bulging. A hematocrit count in the physiological range (HCT = 24%) was considered, and a constant pressure drop was used to drive the flow for all Cases. The well-known Fåhræus and Fåhræus–Lindqvist effects are reproduced, showing the migration of RBCs to the central region of the vessel while forming a cell-free layer near the vessel wall.

The dynamics of a single cell with an initial peripheral location results in radial migration with a swinging motion until reaching the vessel centre, where a stable parachute shape is maintained. For cases with physiological HCT, RBC dynamics reveals phenomena that include ceaseless radial migration, vacillating between the core and wall of the vessel. At different radial locations, the shape, stretch ratio and orientation of RBCs vary preferentially. In the 'middle' radial partition a small standard deviation of the measures is recorded, indicating that in this region of the vessel lumen the RBCs behave in a similar fashion.

The sophisticated, unsteady dynamics of the RBCs is brought on by the complex flow field, which is in turn induced by the intercellular fluid mechanics interaction as well as the RBC deformability property. By decomposing the velocity flow field into a dominant coaxial velocity and a secondary velocity field, relative to an individual RBC (a Lagrangian reference frame, see Eq. (5)), the complex flow field clearly emerges. For example, in the simulation of Case 1 for a single RBC, a trailing vortex ring is generated behind the stable parachute shape configuration. Other more complex flow field examples with physiological hematocrit values are also reported.

In the central region of the vessel where RBCs cluster, the dynamic interplay between the cells can be interpreted as a continual rearrangement to fit in the downstream wake of the preceding RBCs. This motion effectively acquires an aggregate behaviour, affecting the local apparent viscosity and momentum dissipation, that is adaptive and dependent on both the flow field's secondary structures and RBC deformability.

The motion of RBCs is seen to affect the distribution of wall shear stress exerted on the vessel walls, both in magnitude and direction. When bulging endothelial cells are modelled (Case 3), the protruding crests of the endothelial cells are seen to bear higher shear stresses, while the interstitial regions are spared from

high stresses. This results in greater uniformity in spatial (and temporal) stress patterns that the flow effectively exerts on the vessel wall, as compared to the smooth circular vessel simulation (Case 2).

The study remains a preliminary work, especially in that idealised geometries were utilised and the same pressure drop was imposed to drive the flow. Future work should include the presence of the glycocalyx, which has been estimated to affect the stresses exerted on the vessel wall (Secomb, 2001, 2002). The inclusion of white blood cells and platelets, together with phenomena of tethering and adhesion, should also be considered in future work since, combined, these will affect the inter-cellular interactions and subsequently also the flow field. Moreover, viscosity differences between plasma and cytoplasm should be considered, and greater experimental data is necessary to improve parameter and modelling choices.

Conflict of interest statement

There are no conflicts of interest to state.

Acknowledgements

The author acknowledges the support from project 'MatCom-Phys' under the European Research Executive Agency FP7-PEOPLE-2011-IEF framework, as well as FCT (Portugal) projects EXCL/MAT-NAN/0114/2012 and BIOMIMETICPTDC/SAU-ENB/116929/2010 and FEDER through COMPETE. The author is grateful to the Faculty of Physics of the Jagiellonian University for providing the excellent facilities which have made this work possible.

Appendix A. Numerical discretisation and scheme

A.1. Moving Particle Semi-implicit (MPS) method: a mesh-free particle-based method

The mesh-free particle-based method employed to solve the incompressible, Navier–Stokes equations is based on the Moving Particle Semi-implicit (MPS) method (Gambaruto, 2015). Therefore, let us consider a scattered set of points, where locally the central particle is located at $\mathbf{x}_i$ and M neighbouring particles have locations $\mathbf{x}_j$ and lie within the compact support r_e. The distance between these particles is given by $r = |\mathbf{x}_j - \mathbf{x}_i|$. In mesh-free methods, function approximation relies on the information available in a local neighbourhood and is commonly formulated as a weighted radial interaction. In the classical MPS method the weight function is given by:

$$w(r) = \begin{cases} \frac{r_e}{r} - 1 & 0 < r < r_e \\ 0 & r_e < r \end{cases} \tag{7}$$

where $r_e = 2.1 h_0$ is commonly chosen.

From these considerations we can smoothly interpolate the value of an arbitrary scalar ϕ at an arbitrary location i by:

$$\phi_i = \frac{1}{\sum_{j\neq i}^{M} w(r)} \sum_{j\neq i}^{M} \left(w(r)\ \phi_j \right) \tag{8}$$

By setting $\phi = 1$, the 'particle number density' at a particle i is given by:

$$n_i = \sum_{j\neq i}^{M} w(r) \tag{9}$$

Since particles represent lumped volumes of fluid, the density is proportional to the particle number, $\rho_i \propto n_i$. For incompressible flows this particle number density should be constant n^0.

A.2. Outline of scheme

The steps involved to compute the solution at the successive time step can be concisely detailed as follows (Gambaruto, 2015):

Step 1. pressure field for pressure boundary conditions (implicit step),

$$\nabla^2 p^* = 0, \quad \text{with BCs}: \ \Delta p \text{ for periodic sections}, \ \nabla p \cdot \vec{\mathbf{n}} = 0 \text{ at walls};$$

Step 2. body forces (pressure gradient, spring forces),

$$\mathbf{f}_p^n = \frac{-1}{\rho} \nabla p^*, \quad \mathbf{g}^n = \text{sum of spring forces};$$

Step 3. solve for the viscous forces and increment velocity (implicit step),

$$\mathbf{u}^* = \mathbf{u}^n + \Delta t(\mathbf{g}^n + \mathbf{f}_p^n) + \Delta t(\nu \nabla^2 \mathbf{u}^*), \quad \text{with BCs}: \ \mathbf{u}_i = 0 \text{ at walls};$$

Step 4. check CFL condition is satisfied, if not go to Step 3 with smaller Δt;

Step 5. move particles,

$$\mathbf{x}^* = \mathbf{x}^n + \Delta t\ \mathbf{u}^*;$$

Step 6. pressure Poisson equation to satisfy incompressibility (implicit step),

$$\nabla^2 p^{n+1} = \frac{-\rho}{\Delta t^2} \frac{(n^* - n^0)}{n^0}, \quad \text{with BCs}: \ \nabla p \cdot \vec{\mathbf{n}} = 0 \text{ at walls};$$

Step 7. update the velocity,

$$\mathbf{u}^{n+1} = \mathbf{u}^* + \mathbf{u}^{**} = \mathbf{u}^* - \frac{\Delta t}{\rho} \nabla p^{n+1};$$

Step 8. move particles,

$$\mathbf{x}^{n+1} = \mathbf{x}^n + \Delta t\ \mathbf{u}^{n+1}.$$

A.3. Discrete differential operators

In order to solve for the Navier–Stokes equations using the above scheme, the derivative terms that appear need to be substituted by discrete differential operators. In the following, let us consider an arbitrary scalar quantity ϕ given at each particle in d spatial dimensions.

The discrete gradient operator is computed as a weighted average over neighbouring particles as:

$$\langle \nabla \phi \rangle_i = \frac{d}{n_i} \sum_{j\neq i}^{M} w(r) \frac{(\phi_j - \phi_i)(\mathbf{x}_j - \mathbf{x}_i)}{|\mathbf{x}_j - \mathbf{x}_i|^2} \tag{10}$$

The discrete Laplacian operator is derived from the solution of the diffusion equation, and is given by:

$$\langle \nabla^2 \phi \rangle_i = \frac{2d}{\lambda n_i} \sum_{j\neq i}^{M} w(r)(\phi_j - \phi_i); \quad \text{where } \lambda = \frac{\sum_{j\neq i}^{M} \left(w(r)\ r^2 \right)}{\sum_{j\neq i}^{M} w(r)} \tag{11}$$

A.4. Membrane dynamics modelled by a spring network

The spring network discretisation for the cell membranes is composed of three spring types, as noted in Eq. (2). These are: tension/compression springs ($\mathbf{f}^t$), bending springs ($\mathbf{f}^b$), and repulsive springs ($\mathbf{f}^r$), which are detailed briefly below following the notation in Fig. 2.

The forces for tension/compression springs act to resist stresses in the plane of the triangle elements:

$$\mathbf{f}_i^t = \kappa_t \frac{(|\mathbf{x}_{ij}| - L_0)}{L_0} \frac{\mathbf{x}_{ij}}{|\mathbf{x}_{ij}|} \tag{12}$$

where κ_t is the spring stiffness, $\mathbf{x}_{ij} = \mathbf{x}_j - \mathbf{x}_i$ is the vector connecting particles i and j, and L_0 is the spring rest length.

Bending springs resist membrane curvature and act orthogonal to the triangle elements (Bridson et al., 2003):

$$\mathbf{f}_j^b = \left(\frac{|E|^2}{|N_1| + |N_2|}\right)(\theta - \theta_0)\, \kappa_b\, \eta_j; \quad \text{for } j = 1, \ldots, 4 \tag{13}$$

with

$$\begin{aligned} \eta_1 &= |E| \frac{N_1}{|N_1|^2}; \quad \eta_3 = \frac{(\mathbf{x}_1 - \mathbf{x}_4)\cdot E}{|E|} \cdot \frac{N_1}{|N_1|^2} + \frac{(\mathbf{x}_2 - \mathbf{x}_4)\cdot E}{|E|} \cdot \frac{N_2}{|N_2|^2} \\ \eta_2 &= |E| \frac{N_2}{|N_2|^2}; \quad \eta_4 = -\frac{(\mathbf{x}_1 - \mathbf{x}_3)\cdot E}{|E|} \cdot \frac{N_1}{|N_1|^2} - \frac{(\mathbf{x}_2 - \mathbf{x}_3)\cdot E}{|E|} \cdot \frac{N_2}{|N_2|^2} \end{aligned} \tag{14}$$

where θ_0 is the rest angle, $N_1 = (\mathbf{x}_1 - \mathbf{x}_3) \times (\mathbf{x}_1 - \mathbf{x}_4)$, $N_2 = (\mathbf{x}_2 - \mathbf{x}_4) \times (\mathbf{x}_2 - \mathbf{x}_3)$, $E = (\mathbf{x}_4 - \mathbf{x}_3)$.

The repulsive forces act on any abutting particle to the membrane:

$$\begin{aligned} \mathbf{f}_j^r &= -\kappa_r\, \hat{\mathbf{n}} \left(\frac{d_e}{x_{4,5}} - 1\right) \frac{A_j}{A} \quad \text{if } 0 < x_{4,5} < d_e; \quad \text{for } j = 1, 2, 3 \\ \mathbf{f}_4^r &= -\sum_{j=1}^{3} \mathbf{f}_j^r \end{aligned} \tag{15}$$

where $x_{4,5} = |\mathbf{x}_4 - \mathbf{x}_5|$, $\hat{\mathbf{n}}$ is the membrane surface unit normal, and d_e is the radius of compact support for the repulsive forces. If $x_{4,5} \geq d_e$ then $\mathbf{f}^r = 0$.

The spring coefficients were set to $\kappa_t = 8 \times 10^4$ m s^{-2}, $\kappa_b = 2 \times 10^{-2}$ m^2 s^{-2}, and $\kappa_r = 4 \times 10^4$ m s^{-2}, with $L_0 = h_0$, $\theta_0 = 0$ and $d_e = h_0$, following benchmarked results for static stretch tests in Gambaruto (2015).

References

Abkarian, M., Faivre, M., Viallat, A., 2007. Swinging of red blood cells under shear flow. Phys. Rev. Lett. 98 (18), 188302.

Alizadehrad, D., Imai, Y., Nakaaki, K., Ishikawa, T., Yamaguchi, T., 2012. Quantification of red blood cell deformation at high-hematocrit blood flow in microvessels. J. Biomech. 45 (15), 2684–2689.

Alizadehrad, D., Imai, Y., Nakaaki, K., Ishikawa, T., Yamaguchi, T., 2012. Parallel simulation of cellular flow in microvessels using a particle method. J. Biomech. Sci. Eng. 7 (1), 57–71.

Bessonov, N., Babushkina, E., Golovashchenko, S.F., Tosenberger, A., Ataullakhanov, F., Panteleev, M., Tokarev, A., Volpert, V., 2014. Numerical modelling of cell distribution in blood flow. Math. Model. Nat. Phenom. 9 (6), 69–84.

Bridson, R., Marino, S., Fedkiw, R., 2003. Simulation of clothing with folds and wrinkles. In: Eurographics/SIGGRAPH Symposium on Computer Animation, pp. 28–36.

Fedosov, D.A., Caswell, B., Karniadakis, G.E., 2010. A multiscale red blood cell model with accurate mechanics, rheology, and dynamics. Biophys. J. 98, 2215–2225.

Fedosov, D.A., Caswell, B., Karniadakis, G.E., 2010. Systematic coarse-graining of spectrin-level red blood cell models. Comput. Methods Appl. Mech. Eng. 199, 1937–1948.

Freund, J.B., Orescanin, M.M., 2011. Cellular flow in a small blood vessel. J. Fluid Mech. 671, 466–490.

Freund, J.B., Vermot, J., 2014. The Wall-stress footprint of blood cells flowing in microvessels. Biophys. J. 106 (3), 752–762.

Fukushima, S., Fujioka, H., Tanishita, K., 2003. Shear stress distribution on the surface of endothelial cells during flow-induced morphological remodeling. JSME Int. J. Ser. C 46 (4), 1275–1283.

Gambaruto, A.M., 2015. Computational haemodynamics of small vessels using Moving Particle Semi-implicit (MPS) method. J. Comput. Phys. 302, 68–96 http://dx.doi.org/10.1016/j.jcp.2015.08.039.

Garipcan, B., Maenz, S., Pham, T., Settmacher, U., Jandt, K.D., Zanow, J., Bossert, J., 2011. Image analysis of endothelial microstructure and endothelial cell dimensions of human arteries-a preliminary study. Adv. Eng. Mater. 13 (1–2), B54–B57.

Imai, Y., Kondo, H., Ishikawa, T., Lim, C.T., Yamaguchi, T., 2010. Modeling of haemodynamics arising from malaria infection. J. Biomech. 43, 1386–1393.

Koshizuka, S., Nobe, A., Oka, Y., 1998. Numerical analysis of breaking waves using the moving particle semi-implicit method. Int. J. Numer. Methods Fluids 26, 751–769.

Lima, R., Ishikawa, T., Imai, Y., Takeda, M., Wada, S., Yamaguchi, T., 2008. Radial dispersion of red blood cells in blood flowing through glass capillaries: the role of hematocrit and geometry. J. Biomech. 41 (10), 2188–2196.

Lipowsky, H.H., 2005. Microvascular rheology and hemodynamics. Microcirculation 12, 5–15.

Meßlinger, S., Schmidt, B., Noguchi, H., Gompper, G., 2009. Dynamical regimes and hydrodynamic lift of viscous vesicles under shear. Phys. Rev. E 80 (1), 011901.

Nix, S., Imai, Y., Matsunaga, D., Yamaguchi, T., Ishikawa, T., 2014. Lateral migration of a spherical capsule near a plane wall in Stokes flow. Phys. Rev. E 90, 043009.

Ohashi, T., Sato, M., 2005. Remodeling of vascular endothelial cells exposed to fluid shear stress: experimental and numerical approach. Fluid Dyn. Res. 37 (1), 40–59.

Omori, T., Ishikawa, T., Barthès-Biesel, D., Salsac, A.V., Walter, J., Imai, Y., Yamaguchi, T., 2011. Comparison between spring network models and continuum constitutive laws: application to the large deformation of a capsule in shear flow. Phys. Rev. E 83, 041918.

Omori, T., Imai, Y., Yamaguchi, T., Ishikawa, T., 2012. Reorientation of a nonspherical capsule in creeping shear flow. Phys. Rev. Lett. 108 (13), 138102.

Omori, T., Imai, Y., Kikuchi, K., Ishikawa, T., Yamaguchi, T., 2015. Hemodynamics in the microcirculation and in microfluidics. Ann. Biomed. Eng. 43 (1), 238–257.

Pan, W., Caswell, B., Karniadakis, G.E., 2010. A low-dimensional model for the red blood cell. Soft Matter 6 (18), 4366–4376.

Popel, A.S., Johnson, P.C., 2005. Microcirculation and hemorheology. Annu. Rev. Fluid Mech. 37, 43–69.

Pries, A.R., Neuhaus, D., Gaehtgens, P., 1992. Blood viscosity in tube flow: dependence on diameter and hematocrit. Am. J. Physiol.—Heart Circul. Physiol. 263 (6), H1770–H1778.

Saffman, P.G.T., 1965. The lift on a small sphere in a slow shear flow. J. Fluid Mech. 22 (2), 385–400.

Secomb, T.W., Hsu, R., Pries, A.R., 2001. Motion of red blood cells in a capillary with an endothelial surface layer: effect of flow velocity. Am. J. Physiol.—Heart Circul. Physiol. 281 (2), H629–H636.

Secomb, T.W., Hsu, R., Pries, A.R., 2002. Blood flow and red blood cell deformation in nonuniform capillaries: effects of the endothelial surface layer. Microcirculation 9 (3), 189–196.

Shepard, D., 1968. A two-dimensional interpolation function for irregularly-spaced data. In: Proceedings of the 1968 ACM National Conference, pp. 517–524.

Suresh, S., Spatz, J., Mills, J.P., Micoulet, A., Dao, M., Lim, C.T., Beil, M., Seufferlein, T., 2005. Connections between single-cell biomechanics and human disease states: gastrointestinal cancer and malaria. Acta Biomater. 1 (1), 15–30.

Takeishi, N., Imai, Y., Nakaaki, K., Yamaguchi, T., Ishikawa, T., 2014. Leukocyte margination at arteriole shear rate. Physiol. Rep. 2, e12037.

Tsubota, K., Wada, S., 2010. Elastic force of a red blood cell membrane during tank-treading motion: consideration of membrane's natural state. Int. J. Mech. Sci. 52, 356–364.

Yamaguchi, T., Yamamoto, Y., Liu, H., 2000. Computational mechanical model studies on the spontaneous emergent morphogenesis of the cultured endothelial cells. J. Biomech. 33 (1), 115–126.